INTERNATIONAL JOURNAL FOR NUMERICAL METHODS IN FLUIDS
Int. J. Numer. Meth. Fluids 2006; **51**:489–510
Published online 20 December 2005 in Wiley InterScience (www.interscience.wiley.com). DOI: 10.1002/fld.1124

Flow effects of blood constitutive equations in 3D models of vascular anomalies

Panagiotis Neofytou[1,*,†] and Sokrates Tsangaris[2,‡]

[1]*Environmental Research Laboratory, INT-RP, National Centre for Scientific Research 'Demokritos', Agia Paraskevi, 15310 Athens, Greece*
[2]*School of Mechanical Engineering, Fluids Section, National Technical University of Athens, Zografou, 15780 Athens, Greece*

SUMMARY

The effects of different blood rheological models are investigated numerically utilizing two three-dimensional (3D) models of vascular anomalies, namely a stenosis and an abdominal aortic aneurysm model. The employed CFD code incorporates the SIMPLE scheme in conjunction with the finite-volume method with collocated arrangement of variables. The approximation of the convection terms is carried out using the QUICK differencing scheme, whereas the code enables also multi-block computations, which are useful in order to cope with the two-block grid structure of the current computational domain. Three non-Newtonian models are employed, namely the Casson, Power-Law and Quemada models, which have been introduced in the past for modelling the rheological behaviour of blood and cover both the viscous as well as the two-phase character of blood. In view of the haemodynamical mechanisms related to abnormalities in the vascular network and the role of the wall shear stress in initiating and further developing of arterial diseases, the present study focuses on the 3D flow field and in particular on the distribution as well as on both low and high values of the wall shear stress in the vicinity of the anomaly. Finally, a comparison is made between the effects of each rheological model on the aforementioned parameters. Results show marked differences between simulating blood as Newtonian and non-Newtonian fluid and furthermore the Power-Law model exhibits different behaviour in all cases compared to the other models whereas Quemada and Casson models exhibit similar behaviour in the case of the stenosis but different behaviour in the case of the aneurysm. Copyright © 2005 John Wiley & Sons, Ltd.

KEY WORDS: haemodynamics; CFD; blood constitutive equations; stenosis; abdominal aortic aneurysm

1. INTRODUCTION

The presence of an abnormality in the human circulatory system may substantially alter the flow field and subsequently the flow rate of blood leading to severe pathological incidences.

*Correspondence to: P. Neofytou, Environmental Research Laboratory, Institute of Nuclear Technology & Radiation Protection, National Center for Scientific Research 'Demokritos', Agia Paraskevi, 15310 Athens, Greece.
†E-mail: panosn@ipta.demokritos.gr
‡E-mail: sgt@fluid.mech.ntua.gr

Received 6 December 2004
Revised 9 February 2005
Accepted 15 September 2005

In the case of a stenosis the consequences may be cardiac arrest and stroke whereas the development of an abdominal aortic aneurysm (AAA) and its continuous dilation may lead to rupture of the diseased vessel posing an extremely high risk of fatality. Furthermore, the presence of the anomaly itself may lead to flow disturbances such as vortex formation, which is reported as a contributing factor to atherogenesis and thrombogenesis [1]. The role of fluid dynamics in the arterial network and furthermore in the development of vascular diseases involving three-dimensional (3D) geometry set-ups has been under investigation for many years.

As regards the flow through a stenosis, Ang and Mazumdar [2] used Computational Fluid Dynamics (CFD) in order to model the flow in a vessel with an asymmetric stenosis and study the shear-stress distribution in the vicinity of the occlusion. Their results show that the peak shear stress varies only slightly with the Reynolds number. Numerical simulation of the flow in an asymmetric geometry was also performed by Dvinsky and Ojha [3] in order to validate their code and complement previous experimental results. Bethier *et al.* [4] numerically solved the flow in a realistic 3D reconstruction of the human right coronary artery focusing on the effects of the reconstruction methods. They showed that the local flow patterns are severely affected by the geometrical modifications. Axisymmetric and asymmetric 3D stenotic models were used by Long *et al.* [5] to study the flow separation zone and the wall shear-stress distribution in the poststenotic region involving three degrees of area reduction and using a realistic pressure waveform as inlet condition. Their results show a complexity of the flow patterns especially in the flow deceleration phase. The phenomenon of wall deformability was taken into account in the study by Tang *et al.* [6] where a 3D computational model with fluid–wall interaction was introduced to investigate the flow in stenotic elastic tubes and to quantify wall collapse and related critical flow attributes and wall mechanical conditions. In addition to numerical modelling, experimental studies regarding stenotic vessels were also performed by Deplano and Siouffi [7] using a water and glycerol mixture to simulate blood viscosity. Their experiments conclude that high shear-stress values at the throat of the constriction can imply more damage as plaque disruptions. Flow visualization experiments in an axisymmetric stenotic vessel were also carried out by Bluestein *et al.* [8] showing that periodic vortex-shedding in the poststenotic region begins at approximately $Re = 375$ and that the unsteady flow development in the recirculation region may be the mechanism for significant changes in the distribution of mural platelet deposition.

As regards the flow through an aneurysm, Oshima *et al.* [9] developed a numerical simulation system employing the finite-element method in order to clinically study the flow in a cerebral aneurysm. Their geometrical model was derived by computed tomography data. The finite-element method was also used by Kumar and Naidu [10] that performed numerical simulations on 2D axisymmetric aneurysm models with 0–75% dilation. Their results are essentially an examination of the sensitivity of various flow parameters to dilation height. In a later study, Kumar [11] employs a 3D model of a vessel with two asymmetric aneurysms to numerically evaluate the wall shear stress and wall pressure within aneurysms and also to analyse the vortex dynamics, which can lead to thrombus formation. Studies of AAAs in particular have been performed by Yu *et al.* [12] who investigated the steady and pulsatile flow characteristics in axisymmetric AAA models using a commercial CFD package. A later study by Yu [13] was solely focused on the experimental investigation of the steady and pulsatile flow in an AAA model using Particle Image Velocimetry. The study covered different model geometries as well as different Reynolds and Womersley numbers. Egelhoff *et al.* [14]

investigated both experimentally and numerically the flow in AAA models during resting and exercise conditions and showed that no vortex formation takes place in small AAAs whereas vortex formation and transition to turbulence takes place in moderate size AAAs under exercise conditions. Transition to turbulence was also addressed in a similar experimental study by Salsac *et al.* [15] who also investigated the magnitude of wall shear stress during progressive enlargement of AAAs. Numerical flow predictions in AAAs were also performed by Viswanathan *et al.* [16] who used a more sophisticated AAA model covering different geometrical parameters and confirmed that mechanical forces on the arterial wall caused by the blood flow may play an important role in both development and growth of aneurysms.

The aim of the present study is to investigate the effects of modelling the blood as non-Newtonian fluid in 3D flows as done in the past for 2D flows [17–20] employing three well-documented blood rheological models namely the Casson [21], Power-Law [22] and Quemada [23] models. The investigation is carried out by numerically modelling the flow in 3D axisymmetric models of a stenosis and an aneurysm at different Reynolds numbers and degrees of severity.

2. MODEL

2.1. Governing equations

The flow is considered to be laminar and incompressible and therefore the Navier–Stokes equations for 3D incompressible flow are used in their integral form in order to accommodate the subsequent finite-volume discretization. The continuity is given by

$$\int_S \mathbf{V} \cdot \mathbf{dS} = 0 \tag{1}$$

where $\mathbf{V} = (u, v, w)$, u, v and w are the velocity components in the x, y and z directions, respectively, and momentum equations

$$\frac{\partial}{\partial t}\int_\Omega \rho u \, \mathrm{d}\Omega + \int_S \rho u \mathbf{V} \cdot \mathbf{dS} = -\int_S p\mathbf{i}_x \cdot \mathbf{dS} + \int_S (\tau_{xx}\mathbf{i}_x + \tau_{yx}\mathbf{i}_y + \tau_{zx}\mathbf{i}_z) \cdot \mathbf{dS} \tag{2a}$$

$$\frac{\partial}{\partial t}\int_\Omega \rho v \, \mathrm{d}\Omega + \int_S \rho v \mathbf{V} \cdot \mathbf{dS} = -\int_S p\mathbf{i}_y \cdot \mathbf{dS} + \int_S (\tau_{xy}\mathbf{i}_x + \tau_{yy}\mathbf{i}_y + \tau_{zy}\mathbf{i}_z) \cdot \mathbf{dS} \tag{2b}$$

$$\frac{\partial}{\partial t}\int_\Omega \rho w \, \mathrm{d}\Omega + \int_S \rho w \mathbf{V} \cdot \mathbf{dS} = -\int_S p\mathbf{i}_z \cdot \mathbf{dS} + \int_S (\tau_{xz}\mathbf{i}_x + \tau_{yz}\mathbf{i}_y + \tau_{zz}\mathbf{i}_z) \cdot \mathbf{dS} \tag{2c}$$

for the x, y and z directions, respectively. Ω represents volume; $\mathbf{dS}$ equals $\mathbf{n} \cdot \mathrm{d}S$, where $\mathbf{n}$ is the unit vector normal to the surface $\mathrm{d}S$; $\mathbf{i}_x, \mathbf{i}_y, \mathbf{i}_z$ are the unit vectors in the x, y and z directions, respectively; p is the pressure and ρ is the density. Following the analysis in Reference [19] the shear-stress tensor in the diffusion terms is expressed in the case of non-Newtonian fluids as

$$\bar{\tau} = \mu(|\bar{\gamma}|)\bar{\gamma} \tag{3}$$

where $\bar{\dot{\gamma}}$ is the shear-rate tensor and μ is the viscosity expressed as a function of the second invariant of $\bar{\dot{\gamma}}$.

The constitutive equations for modelling the shear thinning attributes of blood are expressed in 3D form as follows:

(i) *Casson model*: Due to its discontinuous character the application of the Casson model [21] in numerical schemes is difficult. Papanastasiou [24] proposed an alternative expression for the whole range of shear-stress values that therefore overcomes this obstacle. Expressed according to (3) this equation becomes

$$\bar{\tau} = \left[\sqrt{\mu_\infty} + \sqrt{\frac{\tau_y}{|\bar{\dot{\gamma}}|}}(1 - \mathrm{e}^{-\sqrt{m|\bar{\dot{\gamma}}|}})\right]^2 \bar{\dot{\gamma}} \tag{4}$$

where τ_y is the yield stress, μ_∞ is the asymptotic viscosity and $m > 100$ for satisfactory approximation. The dimensionless expression of (4) is

$$\bar{\tau}^* = \frac{1}{Re_{\mathrm{CA}}}\left[1 + \sqrt{\frac{Bi}{|\bar{\dot{\gamma}}|^*}}(1 - \mathrm{e}^{-\sqrt{m'|\bar{\dot{\gamma}}|^*}})\right]^2 \bar{\dot{\gamma}}^* \tag{5}$$

where the asterisk superscript denotes dimensionless quantities and

$$Re_{\mathrm{CA}} = \frac{\rho U_\infty D}{\mu_\infty}, \quad Bi = \frac{\tau_y D}{\mu_\infty U_\infty} \tag{6}$$

are the Reynolds and Bingham numbers, respectively, and are the characteristic parameters for a Casson-model flow.

(ii) *Power-Law model*: Based on this model, Walburn and Schneck [22] developed a constitutive equation for blood where in exponent n and parameter k of the model the Total Plasma Minus Albumin (TPMA) and the Haematocrit are taken into account. According to (3) the 3D dimensionless expression is

$$\bar{\tau}^* = \frac{1}{Re_{\mathrm{PL}}}|\bar{\dot{\gamma}}|^{*^{n-1}}\bar{\dot{\gamma}}^* \tag{7}$$

where

$$Re_{\mathrm{PL}} = \frac{\rho D^n}{k U_\infty^{n-2}} \tag{8}$$

is the Reynolds number and characteristic parameter for a Power-Law-model flow.

(iii) *Quemada model*: This model is developed by Quemada [23] for concentrated disperse systems. Based on (3) the 3D expression of the model becomes

$$\bar{\tau} = \mu_{\mathrm{F}}\left(1 - \frac{1}{2}\frac{k_0 + k_\infty\sqrt{|\bar{\dot{\gamma}}|}/\dot{\gamma}_{\mathrm{c}}}{1 + \sqrt{|\bar{\dot{\gamma}}|}/\dot{\gamma}_{\mathrm{c}}}\varphi\right)^{-2}\bar{\dot{\gamma}} \tag{9}$$

where μ_F is the viscosity of plasma (suspending medium), φ is haematocrit and γ_c, k_∞, k_0 are parameters determining the rheological behaviour of the model. The dimensionless expression of (9) is

$$\bar{\tau}^* = \frac{1}{Re_{QU}}\left(1 - \frac{1}{2}\frac{k_0 + k_\infty\sqrt{|\bar{\gamma}|^*/\gamma_c^*}}{1+\sqrt{|\bar{\gamma}|^*/\gamma_c^*}}\varphi\right)^{-2}\bar{\gamma}^* \tag{10}$$

where

$$Re_{QU} = \frac{\rho U_\infty D}{\mu_F}, \quad \gamma_c^* = \frac{\gamma_c}{U_\infty/D} \tag{11}$$

are the characteristic parameters for a Quemada-model flow.

2.2. Geometry

The geometry consists of a tube of diameter D and can be divided into three segments: namely the inlet segment, the deformed segment and the outlet segment. In the case of the stenosis the lengths of the aforementioned segments are equal to $4D, 2D$ and $20D$, respectively, whereas in the case of the aneurysm these are $4D, 4D$ and $18D$, respectively. The radius R_0 of the inlet and outlet segments is undeformed and equal to $D/2$.

In the case of the stenosis the radius of the constricted segment is given by

$$R = R_0\left(1 - \mathrm{St}\left(\frac{1-\cos(\pi x/D)}{2}\right)^2\right), \quad 0 \leqslant x \leqslant 2D \tag{12}$$

where x is measured from the start of the stenosis and St is the degree of the stenosis defined by

$$\mathrm{St} = \frac{R_0 - R_{\min}}{R_0} \tag{13}$$

and $R_{\min}$ is the radius of the tube at the throat of the constriction. For the current study, three different degrees of stenosis were used namely $20, 50$ and 80% (i.e. $0.2, 0.5$ and 0.8, respectively, according to (13)), the shape of which is shown in Figure 1.

In the case of the aneurysm the radius of the deformed segment is given by

$$R = R_0 + (a - R_c + \sqrt{R_c^2 - [b/2 - x]^2}), \quad 0 \leqslant x \leqslant b \tag{14}$$

where x is measured from the start of the dilated segment,

$$R_c = \frac{a^2 + (b/2)^2}{2a}$$

and a is the maximum width of the dilated segment. For the current study, three different values of a were used namely $0.25, 0.4$ and 0.55 corresponding to $D_{\max}/D_0$ values equal to $1.5, 1.8$ and 2.1. The geometry of the aneurysm is shown in Figure 2.

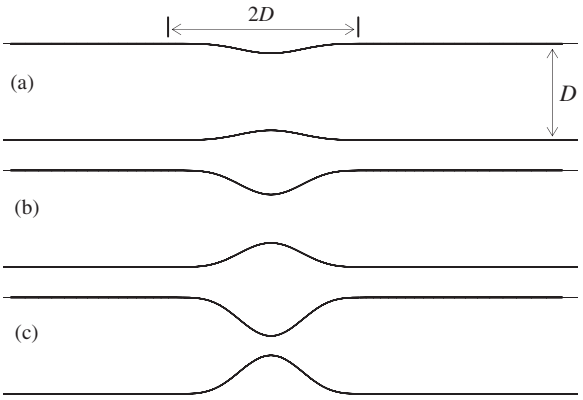

Figure 1. Different degrees of stenosis: (a) 20%; (b) 50%; and (c) 80%.

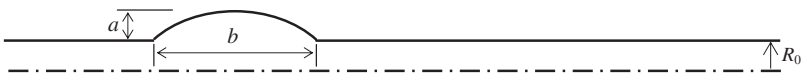

Figure 2. Geometrical model of the vessel with the aneurysm.

2.3. *Conditions and parameters*

Apart from the different degrees of the abnormality, the effects of the blood rheological models under consideration are studied for different Reynolds numbers. They are $Re = 100$, 200 and 300 for the case of the stenosis and $Re = 300$, 900 and 1500 in the case of the aneurysm. Due the fact that the Navier–Stokes equations are incorporated into the numerical scheme in their dimensionless form, the characteristic parameters in Equations (6), (8) and (11) are to be calculated accordingly. For the Casson model and according to Charm *et al.* [25] for blood, $\tau_y = 10.82$ mPa, $\mu_\infty = 3.1 \times 10^{-3}$ Pa s and $\rho = 1056\,\mathrm{kg/m^3}$. In addition, $D = 8$ mm was considered in the case of stenosis in compliance with blood flow in carotid arteries [6] and $D = 2$ cm for the case of aneurysm in compliance with blood flow in AAAs [14]. Therefore, from Re_{CA} having the same definition as Re for Newtonian flows, the calculation of U_∞ from each of the aforementioned values of Re is possible and thus Bi can be calculated. For the Power-Law model the parameters in (8) according to Walburn and Schneck [22] are in the case of blood $k = 14.67 \times 10^{-3}$ Pa s^n and $n = 0.7755$. Therefore according to calculation of U_∞, for each value of Re the corresponding value of Re_{PL} can be calculated. The parameters of Quemada model for blood and for haematocrit $\varphi = 0.45$ are $\gamma_{\mathrm{c}} = 1.88\,\mathrm{s^{-1}}$, $k_\infty = 2.07$ and $k_0 = 4.33$ [23]. Therefore, in the same way as for the other models, the values of Re_{QU} and γ_{c}^* can be calculated. As D, ρ and μ_∞ are constant, the different Re values essentially correspond to different inlet flow rates, whose mean value is U_∞.

The boundary conditions are constant velocity profile and pressure at the inlet and no-slip condition at the walls. At the outlet boundary the pressure and velocity are derived by extrapolation from the inner nodes. The velocity profile at the inlet is regarded to be that of the fully developed flow in a straight tube and can be derived analytically for Newtonian and

Power-Law flows. Its form is

$$\frac{u}{\bar{u}} = 2\left[1 - \left(\frac{r}{R_0}\right)^2\right], \quad 0 \leqslant r \leqslant R_0 \tag{15}$$

for the Newtonian case and

$$\frac{u}{\bar{u}} = \frac{3n+1}{n+1}\left[1 - \left(\frac{r}{R_0}\right)^{(n+1)/n}\right], \quad 0 \leqslant r \leqslant R_0 \tag{16}$$

for the Power-Law case. Due to the complex nature of the equations for the Quemada and Casson models, the fully developed flow used as inlet conditions for each of these cases is calculated numerically similarly as in Reference [26].

3. NUMERICAL METHOD

3.1. Computational scheme

The solution of the equations that model the problem is based on the finite-volume scheme with a collocated arrangement of variables in conjunction with the SIMPLE algorithm. The typical computational topology for a collocated arrangement of variables is shown in Figure 3(a) with a central control volume (CV) with centre P and its neighbouring CVs with centres E, W, N, S, T and B. The equations are solved through an iterative procedure. Rewriting Equations (1) and (2) in non-dimensional form and omitting the asterisk superscript yields

$$\int_S \mathbf{V} \cdot \mathbf{dS} = 0 \tag{17}$$

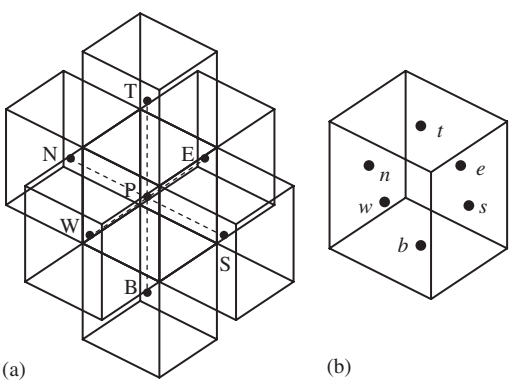

Figure 3. Topology of: (a) grid with collocated arrangement of variables; and (b) control volume.

$$Str\frac{\partial}{\partial t}\int_\Omega u\,\mathrm{d}\Omega+\int_S u\mathbf{V}\cdot\mathbf{dS}$$
$$=-\int_S p\mathbf{i}_x\cdot\mathbf{dS}+\frac{1}{\rho U_\infty D}\int_S\mu\left(\nabla u+\frac{\partial u}{\partial x}\mathbf{i}_x+\frac{\partial v}{\partial x}\mathbf{i}_y+\frac{\partial w}{\partial x}\mathbf{i}_z\right)\cdot\mathbf{dS} \tag{18a}$$

$$Str\frac{\partial}{\partial t}\int_\Omega v\,\mathrm{d}\Omega+\int_S v\mathbf{V}\cdot\mathbf{dS}$$
$$=-\int_S p\mathbf{i}_y\cdot\mathbf{dS}+\frac{1}{\rho U_\infty D}\int_S\mu\left(\nabla v+\frac{\partial u}{\partial y}\mathbf{i}_x+\frac{\partial v}{\partial y}\mathbf{i}_y+\frac{\partial w}{\partial y}\mathbf{i}_z\right)\cdot\mathbf{dS} \tag{18b}$$

$$Str\frac{\partial}{\partial t}\int_\Omega w\,\mathrm{d}\Omega+\int_S w\mathbf{V}\cdot\mathbf{dS}$$
$$=-\int_S p\mathbf{i}_z\cdot\mathbf{dS}+\frac{1}{\rho U_\infty D}\int_S\mu\left(\nabla w+\frac{\partial u}{\partial z}\mathbf{i}_x+\frac{\partial v}{\partial z}\mathbf{i}_y+\frac{\partial w}{\partial z}\mathbf{i}_z\right)\cdot\mathbf{dS} \tag{18c}$$

where $Str=D/U_\infty T$ is the Strouhal number and T is a characteristic time length.

The discretization method will be analysed for the continuity equation (17) and the x-momentum equation (18a) whereas the analysis for (18b) and (18c) is similar. For the discretization of the unsteady term on the CV with centre P (Figure 3) a first-order scheme is introduced, thus

$$\frac{\partial}{\partial t}\int_\Omega u\,\mathrm{d}\Omega\approx\frac{\Delta\Omega}{\Delta t}(u_\mathrm{P}-u_\mathrm{P}^n) \tag{19}$$

For the discretization of the other terms in (18a) the surface integrals may be split into four CV face integrals. Attention will be focused on face 'e' (Figures 3(b) and 4) and the other faces are assumed to be treated in the same way.

In discretizing the convection term, the mass flux through face 'e' is evaluated using existing known velocity

$$\dot{m}_\mathrm{e}^m=\int_{S_\mathrm{e}}\mathbf{V}\cdot\mathbf{dS}\approx u_\mathrm{e}^{m-1}S_\mathrm{e} \tag{20}$$

where u_e^{m-1} can be calculated by linear interpolation between u_P^{m-1} and u_E^{m-1}; m and $m-1$ denote the current and previous iterations, respectively. Hence the convection term becomes

$$\int_{S_\mathrm{e}}u\mathbf{V}\cdot\mathbf{dS}\approx\dot{m}_\mathrm{e}u_\mathrm{e} \tag{21}$$

The value of u_e can be calculated using QUICK [27] scheme, which is third-order accurate and therefore reduces the problem of numerical diffusion compared to lower-order schemes.

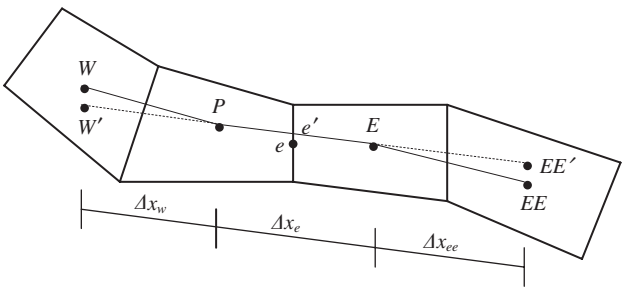

Figure 4. Grid topology for the QUICK scheme.

For the cell face 'e' (Figure 4) the expression for velocity yields.

$$u_{\mathrm{e}}^{\mathrm{QUICK}} = \begin{cases} u_{\mathrm{P}} + C_1^{+}(u_{\mathrm{P}} - u_{\mathrm{W}'})^{m-1} + C_2^{+}(u_{\mathrm{E}} - u_{\mathrm{P}})^{m-1} + \mathrm{d}u_{\mathrm{e}} & \text{if } \dot{m}_{\mathrm{e}} > 0 \\ u_{\mathrm{P}} + C_1^{-}(u_{\mathrm{E}} - u_{\mathrm{EE}'})^{m-1} + C_2^{-}(u_{\mathrm{P}} - u_{\mathrm{E}})^{m-1} + \mathrm{d}u_{\mathrm{e}} & \text{if } \dot{m}_{\mathrm{e}} < 0 \end{cases} \tag{22}$$

where

$$\mathrm{d}u_{\mathrm{e}} = \left(\frac{\partial u}{\partial x}\right)_{\mathrm{e}}^{m-1}(x_{\mathrm{e}} - x_{\mathrm{e}'}) + \left(\frac{\partial u}{\partial y}\right)_{\mathrm{e}}^{m-1}(y_{\mathrm{e}} - y_{\mathrm{e}'}) + \left(\frac{\partial u}{\partial z}\right)_{\mathrm{e}}^{m-1}(z_{\mathrm{e}} - z_{\mathrm{e}'})$$

and

$$\begin{aligned} C_1^{+} &= \frac{\Delta x_{\mathrm{e}}^2}{4(\Delta x_{\mathrm{w}} + \Delta x_{\mathrm{e}})\Delta x_{\mathrm{w}}}, \quad C_1^{-} = \frac{\Delta x_{\mathrm{e}}^2}{4(\Delta x_{\mathrm{e}} + \Delta x_{\mathrm{ee}})\Delta x_{\mathrm{ee}}} \\ C_2^{+} &= \frac{2\Delta x_{\mathrm{w}} + \Delta x_{\mathrm{e}}}{4(\Delta x_{\mathrm{w}} + \Delta x_{\mathrm{e}})}, \quad C_2^{-} = \frac{2\Delta x_{\mathrm{ee}} + \Delta x_{\mathrm{e}}}{4(\Delta x_{\mathrm{e}} + \Delta x_{\mathrm{ee}})} \end{aligned} \tag{23}$$

Therefore the discretized form of the convection term is

$$\int_{S_{\mathrm{e}}} \rho u \mathbf{V} \cdot \mathbf{dS} \approx \rho u_{\mathrm{e}}^{\mathrm{QUICK}} \dot{m}_{\mathrm{e}} \tag{24}$$

where the first term (u_{P}) in (22) is calculated implicitly whereas the remaining terms (superscript $m-1$) are treated as source terms.

Calculation of the diffusive term requires rewriting the term as

$$\int_{S_{\mathrm{e}}} \mu\left(\nabla u + \frac{\partial u}{\partial x}\mathbf{i}_x + \frac{\partial v}{\partial x}\mathbf{i}_y + \frac{\partial w}{\partial x}\mathbf{i}_z\right) \cdot \mathbf{dS} = \underbrace{\int_{S_{\mathrm{e}}} \mu \frac{\partial u}{\partial n}\,\mathrm{d}S}_{A} + \underbrace{\int_{S_{\mathrm{e}}} \mu\left[\frac{\partial u}{\partial x}, \frac{\partial v}{\partial y}, \frac{\partial w}{\partial z}\right] \cdot \mathbf{n}\,\mathrm{d}S}_{B} \tag{25}$$

where n is the direction perpendicular to dS and $\mathbf{n}$ is the corresponding unit vector. It can be assumed that $\partial u/\partial n \approx \partial u/\partial \xi$ where ξ//PE and therefore

$$\underbrace{\int_{S_{\mathrm{e}}} \mu \frac{\partial u}{\partial \xi}\,\mathrm{d}S}_{A'} \approx \mu_{\mathrm{e}} \frac{u_{\mathrm{E}} - u_{\mathrm{P}}}{\mathrm{PE}} S_{\mathrm{e}}$$

The introduced error can be handled using deferred correction that is by expressing the diffusion term (DT) as $A'^m + (A + B - A')^{m-1}$ or

$$\mathrm{DT} = \mu_\mathrm{e} \frac{u_\mathrm{E} - u_\mathrm{P}}{\mathrm{PE}} S_\mathrm{e} + \mu_\mathrm{e} \left\{ \left[2 \left(\frac{\partial u}{\partial x} \right)_\mathrm{e} S_\mathrm{e}^x + \left(\frac{\partial u}{\partial y} + \frac{\partial v}{\partial x} \right)_\mathrm{e} S_\mathrm{e}^y + \left(\frac{\partial u}{\partial z} + \frac{\partial w}{\partial x} \right)_\mathrm{e} S_\mathrm{e}^z \right] - \int_{S_\mathrm{e}} \frac{\partial u}{\partial \xi} \, \mathrm{d}S \right\}^{m-1} \tag{26}$$

where the superscripts x, y, z denote vector components e.g. $S_\mathrm{e}^x = \mathbf{i}_x \cdot \mathbf{S}_\mathrm{e}$. The term noted as $m - 1$ is considered as source term.

The pressure term of the x-momentum equation corresponding to the whole CV (Figure 3(a)) is discretized as

$$- \int_S p \mathbf{i}_x \cdot \mathbf{dS} \approx -(p_\mathrm{e} S_\mathrm{e}^x - p_\mathrm{w} S_\mathrm{w}^x + p_\mathrm{n} S_\mathrm{n}^x - p_\mathrm{s} S_\mathrm{s}^x + p_\mathrm{t} S_\mathrm{t}^x - p_\mathrm{b} S_\mathrm{b}^x)^{m-1} \tag{27}$$

where the values of p can be linear interpolation between the neighbouring nodes (e.g. p_e^{m-1} can be calculated by linear interpolation between p_P^{m-1} and p_E^{m-1}).

If the aforementioned approximations are substituted into (18a) the following algebraic equation is obtained

$$A_\mathrm{P}^x u_\mathrm{P} + \sum_i A_i^x u_i = Q_\mathrm{P}^x, \quad i = \mathrm{T, B, E, W, N, S} \tag{28}$$

where A_i are the coefficients of the unknowns and Q_P are the source terms containing all known terms arising from the discretization.

The coefficients for the y- and z-momentum equations (18b) and (18c) are obtained in a similar fashion yielding a discretized equation similar to (28):

$$A_\mathrm{P}^y v_\mathrm{P} + \sum_i A_i^y v_i = Q_\mathrm{P}^y, \quad i = \mathrm{T, B, E, W, N, S} \tag{29}$$

$$A_\mathrm{P}^z w_\mathrm{P} + \sum_i A_i^z w_i = Q_\mathrm{P}^z, \quad i = \mathrm{T, B, E, W, N, S} \tag{30}$$

For solving the flow and pressure field the SIMPLE method is applied. In the first step of the method a pressure (p^{m-1}) and a velocity field ($u^{m-1}, v^{m-1}, w^{m-1}$) are guessed. Then the discretized momentum equations (28)–(30) are solved using the guessed field to yield the velocity components u^*, v^*, w^*. These values do not generally satisfy mass conservation on each CV. Therefore the velocities u^*, v^* and w^* need to be corrected as follows:

$$u^m = u^* + u', \quad v^m = v^* + v', \quad w^m = w^* + w' \tag{31}$$

and the final values in the m iteration should also satisfy the momentum equation. This is possible only if the pressure is also corrected

$$p^m = p^{m-1} + p' \tag{32}$$

Expressing the velocity on cell face e in terms of the discretized x-momentum equation one can obtain two equations for each of u^* and u^m. Subtracting these equations yields

$$u'_\mathrm{e} = \tilde{u}_\mathrm{e} - C_\mathrm{e}(p'_\mathrm{E} - p'_\mathrm{P}) S_\mathrm{e} \tag{33}$$

where

$$\tilde{u}_{\mathrm{e}} = \bar{u}_{\mathrm{e}}^{m} - \bar{u}_{\mathrm{e}}^{*} + C_{\mathrm{e}}\left[\left(\overline{\int_S p\mathbf{i}_x \cdot \mathbf{dS}}\right)^{m} - \left(\overline{\int_S p\mathbf{i}_x \cdot \mathbf{dS}}\right)^{m-1}\right] \tag{34}$$

and where ($\bar{}$) denotes interpolated value between nodes P and E and C_{e} accounts for geometric properties of the current CV. The corrected velocities are required to satisfy the continuity equation. If the mass flux through cell face 'e' is

$$\dot{m}_{\mathrm{e}} = u_{\mathrm{e}}^{m} S_{\mathrm{e}} = (u_{\mathrm{e}}^{*} + u_{\mathrm{e}}')S_{\mathrm{e}} \tag{35}$$

then a similar expression for the rest of the CV faces yields

$$\sum_c \dot{m}_c = \Delta\dot{m}^{*} + \Delta\dot{m}' = 0, \quad c = \mathrm{t, b, e, w, n, s} \tag{36}$$

Substituting the term $\Delta\dot{m}'$ in (36) as in (33) yields

$$A_{\mathrm{P}} p_{\mathrm{P}}' + \sum_i A_i p_i' = -\Delta\dot{m}^{*} - \Delta\tilde{\dot{m}}, \quad i = \mathrm{T, B, E, W, N, S}, \tag{37}$$

where A are the coefficients of the unknown variables resulting from the discretized expressions for the pressure corrections. If the last term on the RHS of (37) is omitted because it involves values, which are not yet known, one obtains the *pressure-correction equation*

$$A_{\mathrm{P}} p_{\mathrm{P}}' + \sum_i A_i p_i' = -\Delta\dot{m}^{*}, \quad i = \mathrm{T, B, E, W, N, S} \tag{38}$$

Applying (38) on all CVs of the domain results to a system of equations, the solutions of which gives the pressure corrections on each computational node. These are used further to correct the velocity values, which will now satisfy the continuity equations. However, they do not satisfy the momentum equations, so another iteration must be performed using the solutions from the previous time step as an initial guess. This iteration procedure continues until reaching the desired accuracy. It should be noted that if the last term on the RHS of (37) is neglected the SIMPLE algorithm may lead to divergence and therefore underrelaxation should be used. The solution of the systems of equations (28)–(30) and (38) is carried out using Stone's method [28].

3.2. Grid

The grid used in the computations consists of hexahedral elements and is based on multiblock structure. The inner block is of a rectangular cross section and is encircled by the outer block as shown in Figure 5. Furthermore, the grid is locally refined at the constricted segment so that the anomalies in the flow field and the wall shear-stress (WSS) distribution caused by the constriction are captured in more detail.

A grid refinement study is also contacted and three grid resolutions were tested namely grid *a* with 39 345 CVs, grid *b* with 77 108 CVs and grid *c* with 104 160 CVs. The test is carried out for Newtonian flow and for a 50% degree of stenosis by comparing the dimensionless WSS (Figure 6). It can be seen that the results for grids *b* and *c* are very close and therefore grid *b* is used for all further computations of this study both for the stenosis and the aneurysm cases.

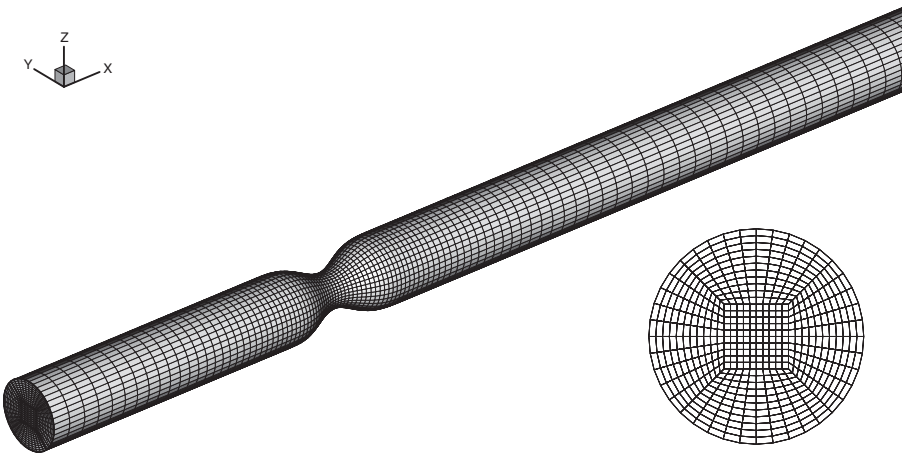

Figure 5. 3D grid with cross-section.

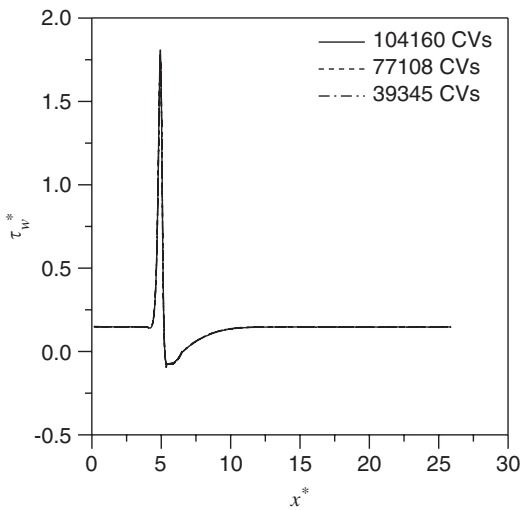

Figure 6. Grid refinement study.

4. RESULTS AND DISCUSSION

Computations are conducted for three different *Re* numbers and three different degrees of abnormality for each case of stenosis and aneurysm so that the effects of a blood rheological model on important flow aspects such as the flow field and WSS distribution are determined. The effects of flow rate are studied by means of different *Re* numbers as follows. Velocity U_∞ is calculated from *Re* (or Re_{CA}) and then used to calculate the rest of the parameters in (6), (8) and (11). Therefore the intercomparison between the models for a specific value of *Re* implies intercomparison for the same inlet flow rate.

4.1. *Effects of flow rate*

4.1.1. Stenosis. The flows for all models corresponding to $Re = 100, 200$ and 300 are simulated according to realistic flow in carotid arteries [6] assuming 50% degree of stenosis. No indication of asymmetry of flow exists as regards the axis of the tube so the results are presented corresponding to a random plane containing the axis. The streamline patterns for the Casson model are shown in Figure 7 where the fashion of growth of the recirculation region with increasing Re is evident. The difference between the vortex-lengths for $Re = 100$ and 200 seems to be the same as that between $Re = 200$ and 300 and that applies to all model cases.

From the pressure-difference (ΔP) between inlet and outlet (Table I) one can see that all non-Newtonian models cause higher pressure-difference than the Newtonian case and implies that a specific pressure difference would induce lower flow rates for the non-Newtonian models. In particular the highest ΔP is induced by the Power-Law model followed by the Casson and then the Quemada models. The change from $Re = 100$ to 200 seems to induce the same rise to ΔP as the change from $Re = 200$ to 300 for all models. Furthermore, the difference between ΔP values for every model at a specific Re seems to be the same for all three Re values.

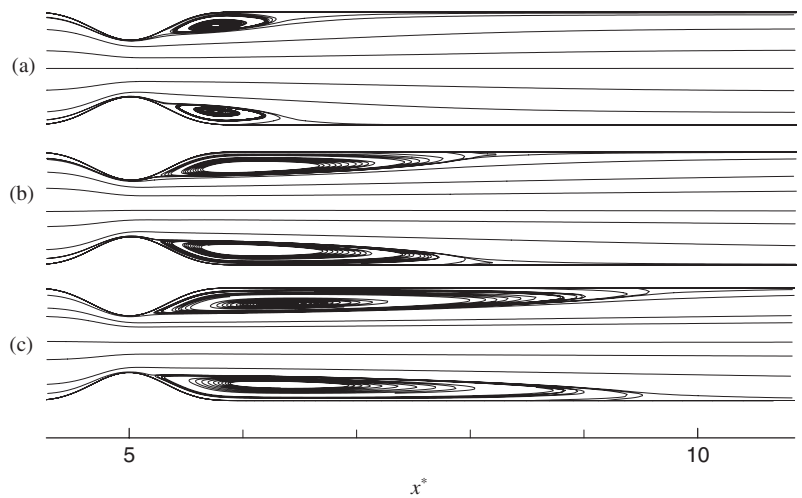

Figure 7. Streamlines for Casson-based flow for: (a) $Re = 100$; (b) $Re = 200$; and (c) $Re = 300$ and for 50% degree of stenosis.

Table I. Pressure difference (in N/m^2) for the various cases of the stenosis flow.

St (%)	*Re*	Newtonian	Casson	Power-Law	Quemada
20	100	12.57	22.62	27.54	19.26
50	100	21.17	31.55	36.52	28.06
50	200	53.05	66.41	72.99	62.02
50	300	95.67	110.39	115.30	105.54
80	100	487.25	493.99	424.83	491.49

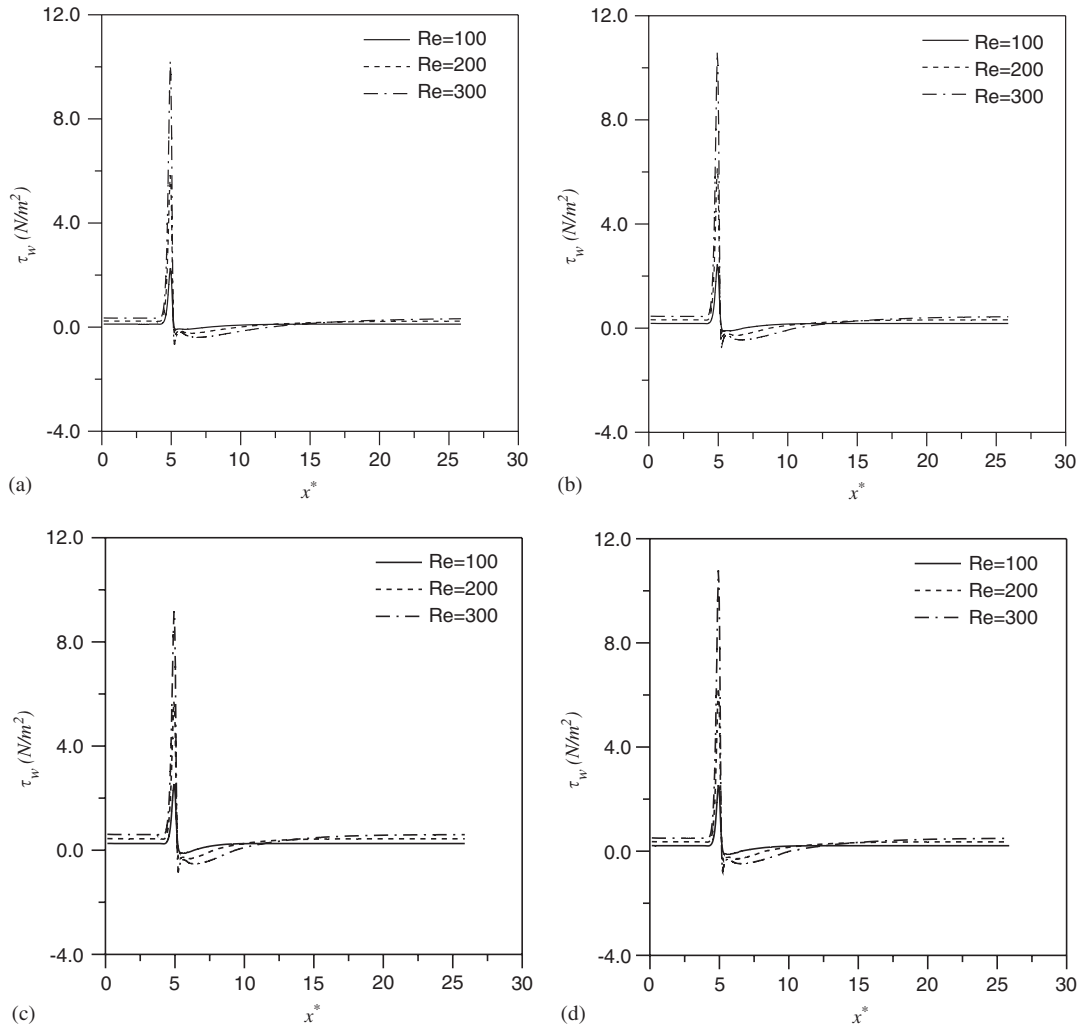

Figure 8. WSS distribution for different *Re* numbers for the stenosis flow for: (a) Newtonian; (b) Casson; (c) Power-Law; and (d) Quemada models.

The distribution of the WSS is one of the most important flow aspects due to its direct relevance to atherosclerosis formation [29]. The distribution of the x-wise component of the WSS is shown in Figure 8 for all models. A prominent positive peak of the distribution is evident at the throat of the constriction, the value of which increases with increasing *Re*. The peak is followed by negative values indicating the presence of the recirculation region and gradually the WSS restores its undisturbed value. The maximum (τ_W^{max}) and minimum (τ_W^{min}) values of the distribution are shown in Table II for all models. For $Re = 100$ the values of τ_W^{min} and τ_W^{max} are very close for all models and higher in absolute compared to the Newtonian case. As *Re* increases the effect differences between the models become more marked and in particular τ_W^{max} for the Power-Law model is lower compared to the rest of the models. This is

Table II. Minimum and maximum wall shear stress (in N/m^2) for the various cases of the stenosis flow.

		Newtonian		Casson		Power-Law		Quemada	
St (%)	*Re*	τ_W^{min}	τ_W^{max}	τ_W^{min}	τ_W^{max}	τ_W^{min}	τ_W^{max}	τ_W^{min}	τ_W^{max}
20	100	4.89e − 2	0.380	0.125	0.523	0.162	0.593	9.88e − 2	0.477
50	100	−8.63e − 2	2.26	−0.110	2.53	−0.108	2.54	−0.102	2.45
50	200	−0.309	5.84	−0.351	6.27	−0.369	5.70	−0.334	6.14
50	300	−0.668	10.21	−0.776	10.78	−0.846	9.17	−0.742	10.61
80	100	−4.42	42.83	−4.58	43.94	−4.48	30.45	−4.54	43.59

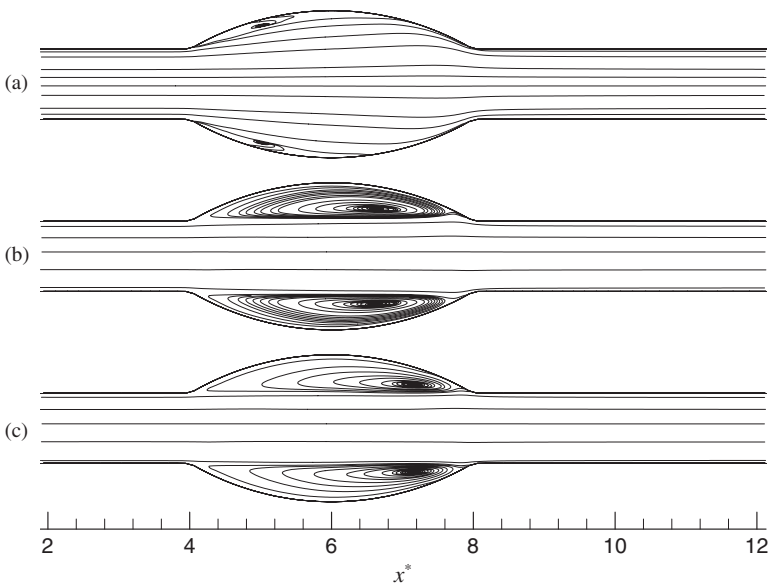

Figure 9. Streamlines for Casson-based flow for: (a) $Re = 300$; (b) $Re = 900$; and (c) $Re = 1500$ and width of aneurysm $a = 0.55$.

induced from the lower viscosity that the Power-Law model exhibits for the high shear-rates occurring at the throat of the constriction due to the velocity gradients becoming more intense for higher *Re*. The value of τ_W^{max} for the Power-Law model also differs markedly from the other models for higher *Re*.

4.1.2. Aneurysm. The flows for all models corresponding to $Re = 300$, 900 and 1500 are simulated assuming $a = 0.55$ width of aneurysm. This range of *Re* numbers covers realistic flow conditions in the abdominal aorta [13, 30]. No indication of asymmetry of flow exists as regards to the axis of the tube so the results are presented corresponding to a random plane containing the axis.

The streamline patterns for the Casson model are shown in Figure 9 where the flow is regarded from left to right. The flow for $Re = 300$ is almost fully attached and the recirculation

Table III. Pressure difference (in N/m^2) for the various cases of the aneurysm flow.

a	Re	Newtonian	Casson	Power-Law	Quemada
0.55	300	5.43	12.21	13.97	9.85
0.55	900	16.96	27.83	34.10	24.33
0.55	1500	29.70	43.52	51.52	38.91
0.40	300	5.43	12.23	13.99	9.86
0.25	300	5.43	12.27	14.05	9.89

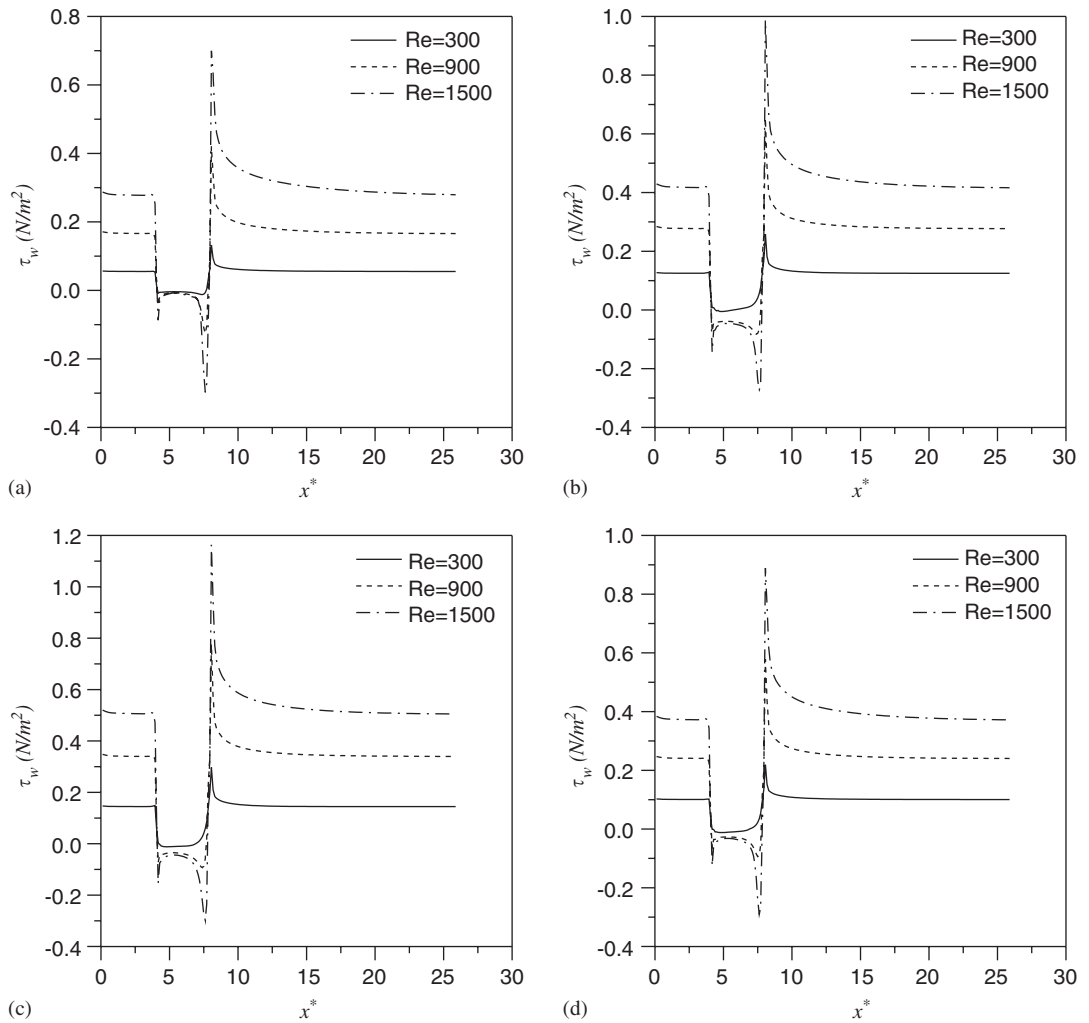

Figure 10. WSS distribution for different Re numbers for the aneurysm flow for: (a) Newtonian; (b) Casson; (c) Power-Law; and (d) Quemada models.

Table IV. Minimum and maximum wall shear stress (in N/m^2) for the various cases of the aneurysm flow.

		Newtonian		Casson		Power-Law		Quemada	
a	Re	τ_W^{min}	τ_W^{max}	τ_W^{min}	τ_W^{max}	τ_W^{min}	τ_W^{max}	τ_W^{min}	τ_W^{max}
0.55	300	−0.012	0.132	−5.32e − 3	0.258	−0.012	0.297	−0.012	0.219
0.55	900	−0.126	0.418	−0.082	0.653	−0.093	0.774	−0.094	0.577
0.55	1500	−0.297	0.696	−0.274	0.983	−0.298	1.162	−0.290	0.886
0.40	300	−7.21e − 3	0.122	6.08e − 3	0.238	−5.28e − 3	0.272	−5.61e − 3	0.201
0.25	300	−4.30e − 3	0.108	0.022	0.209	0.016	0.240	9.54e − 3	0.176

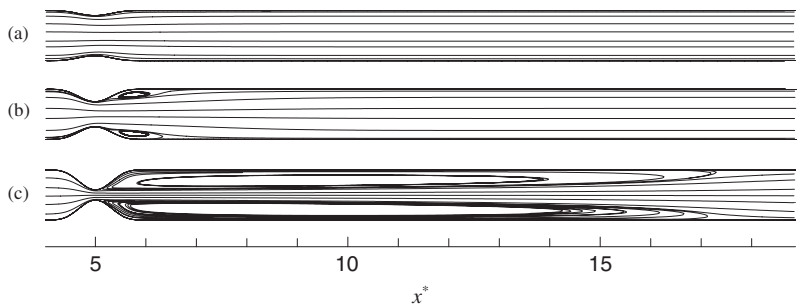

Figure 11. Streamlines for Casson-based flow at $Re = 100$ and for different degrees of stenosis: (a) 20%; (b) 50%; and (c) 80%.

zone is barely formed. For $Re = 900$ the recirculation zone is covering the dilated segment whereas the core flow does not expand within the bulge as for $Re = 300$. As Re increases further ($Re = 1500$) the area of the recirculation zone remains unaltered whereas the vortex center moves downstream towards the exit from the aneurysm.

From the pressure-difference (ΔP) between inlet and outlet (Table III) one can see that all non-Newtonian models cause higher pressure-difference than the Newtonian case and that implies that a specific pressure difference would induce lower flow rates for the non-Newtonian models. In particular the highest ΔP is induced by the Power-Law model followed by the Casson and then the Quemada models. The change from $Re = 300$ to 900 seems to induce approximately the same rise to ΔP as the change from $Re = 900$ to 1500 for all models.

The distribution of the x-wise component of the WSS is shown in Figure 10 for all models. The WSS drops as the flow enters the bulge whereas a prominent positive peak of the distribution is evident at the end of the dilated segment, the value of which increases with increasing Re. For high Re numbers the drop of WSS within the bulge reaches negative values indicating the presence of the recirculation region. As the flow exits the bulge the WSS restores gradually its undisturbed value. The maximum (τ_W^{max}) and minimum (τ_W^{min}) values of the distribution are shown in Table IV for all models. For $Re = 300$ the values of τ_W^{min} are very close for all models and similar to the Newtonian case whereas the values of τ_W^{max} are highest for the Power-Law followed gradually by the Casson and the Quemada models. All aforementioned values of τ_W^{max} are substantially higher than for the Newtonian case. As far as τ_W^{min} is concerned the same yields for higher values of Re whereas the increase of Re induces

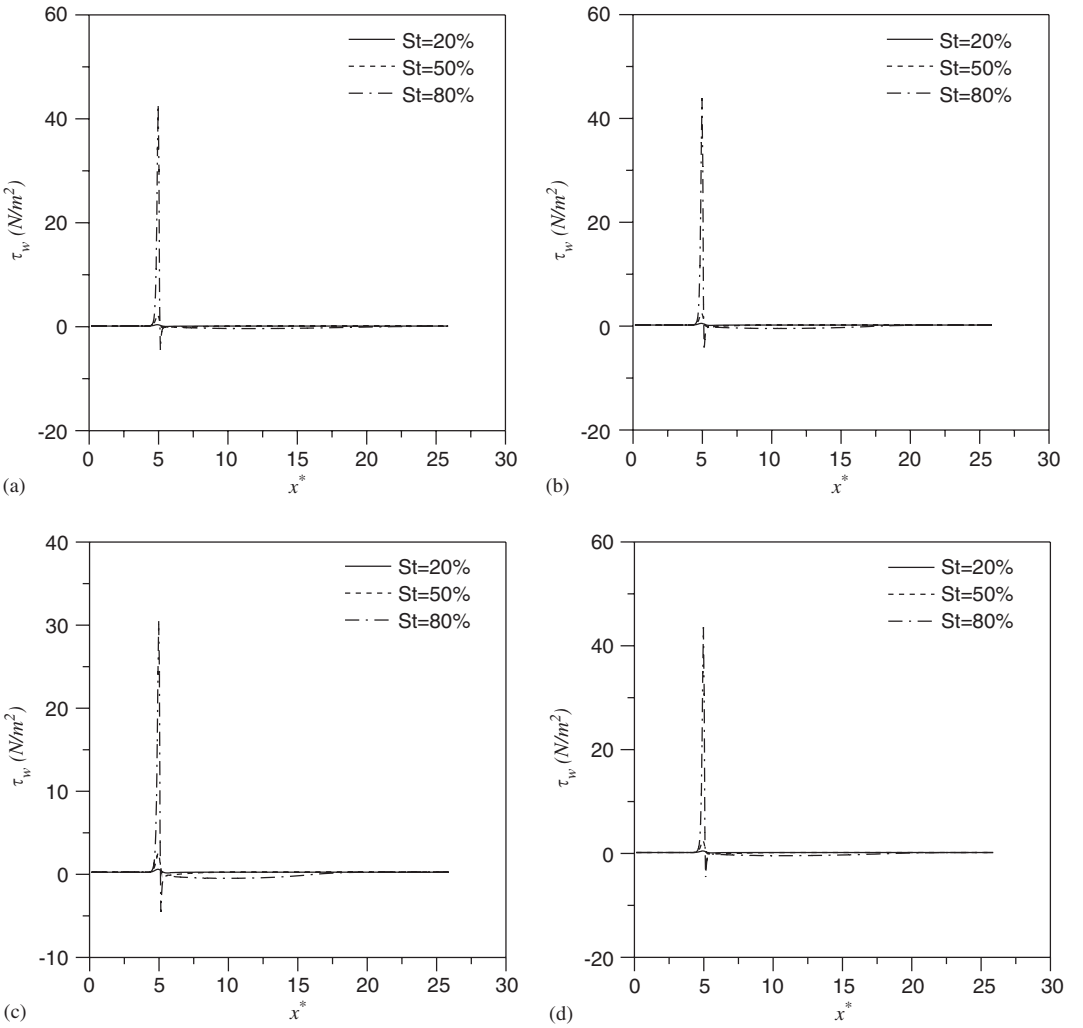

Figure 12. WSS distribution for different degrees of stenosis for: (a) Newtonian; (b) Casson; (c) Power-Law; and (d) Quemada models.

lower values of τ_W^{min} for the Newtonian case compared to the other models for which the values of τ_W^{min} are very close.

4.2. *Effects of abnormality degree*

4.2.1. Stenosis. The flows for all models corresponding to $Re = 100$ and degrees of stenosis equal to 20, 50 and 80% are simulated. The streamlines for the Casson model in Figure 11 show the marked effects that the degree of stenosis has on the flow field. Whereas for 20% stenosis there is no vortex formed and even for 50% stenosis there is a small recirculation zone, for 80% stenosis the recirculation zone is dominant in the flow field.

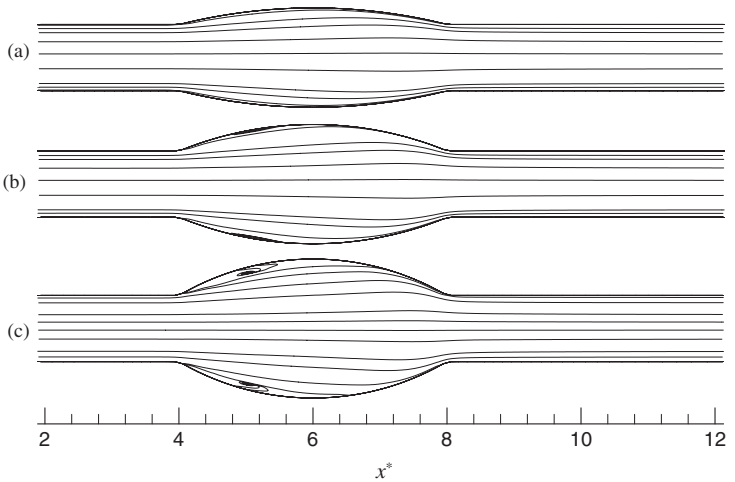

Figure 13. Streamlines for Casson-based flow for different aneurysm widths: (a) $a = 0.25$; (b) $a = 0.40$; and (c) $a = 0.55$ and $Re = 300$.

The different impact that the severity of the stenosis has on the different model flows is more evident in the ΔP results (Table I). It can be seen that although for $\mathrm{St} = 20\%$ the value of ΔP is the highest for the Power-Law model followed by the Casson and then the Quemada models, it becomes the lowest for $\mathrm{St} = 80\%$. Taking into account that the pressure difference is the integral of the WSS over the entire wall of the tube, this phenomenon is directly attributed to the low peak of WSS at the throat of the stenosis that the Power-Law model exhibits compared to the other models (Figure 12). The Quemada and Casson models show similar trends for all degrees of stenosis. This can also be seen in Table II in addition with the results for $\tau_{\mathrm{W}}^{\min}$. The latter is at the same levels for all models when a recirculation zone is formed ($\mathrm{St} = 50, 80\%$). It is worthwhile mentioning that for a change of 30% in the degree of stenosis from 50 to 80% the increase in $\tau_{\mathrm{W}}^{\max}$ is approximately 10 times greater than for the same change from 20 to 50% for all models.

4.2.2. Aneurysm. The flows for all models corresponding to $Re = 300$ and aneurysm width equal to $a = 0.25, 0.40$ and 0.55 are simulated. The streamlines for the Casson model in Figure 13 show the effects that the degree of aneurysm width has on the flow field. It can be seen that for $a = 0.25$ the flow is fully attached and the recirculation zone forms progressively for $a > 0.4$. As shown in Table III the severity of the bulge shows no effect on ΔP for any of the models. ΔP remains highest for the Power-Law model followed gradually by the Casson, Quemada and Newtonian models but the increase of dilation leaves ΔP for every model virtually unaffected. Taking into account that the pressure difference is directly related to the integral of the WSS on the entire area of the wall, one should not expect considerable effects of the bulge increase on the WSS distribution. Indeed as shown in Figure 14 the WSS distribution for the Newtonian case remains virtually unaffected whereas the maximum and minimum levels for the rest of the models exhibit a very small change. The latter can also be seen in Table IV.

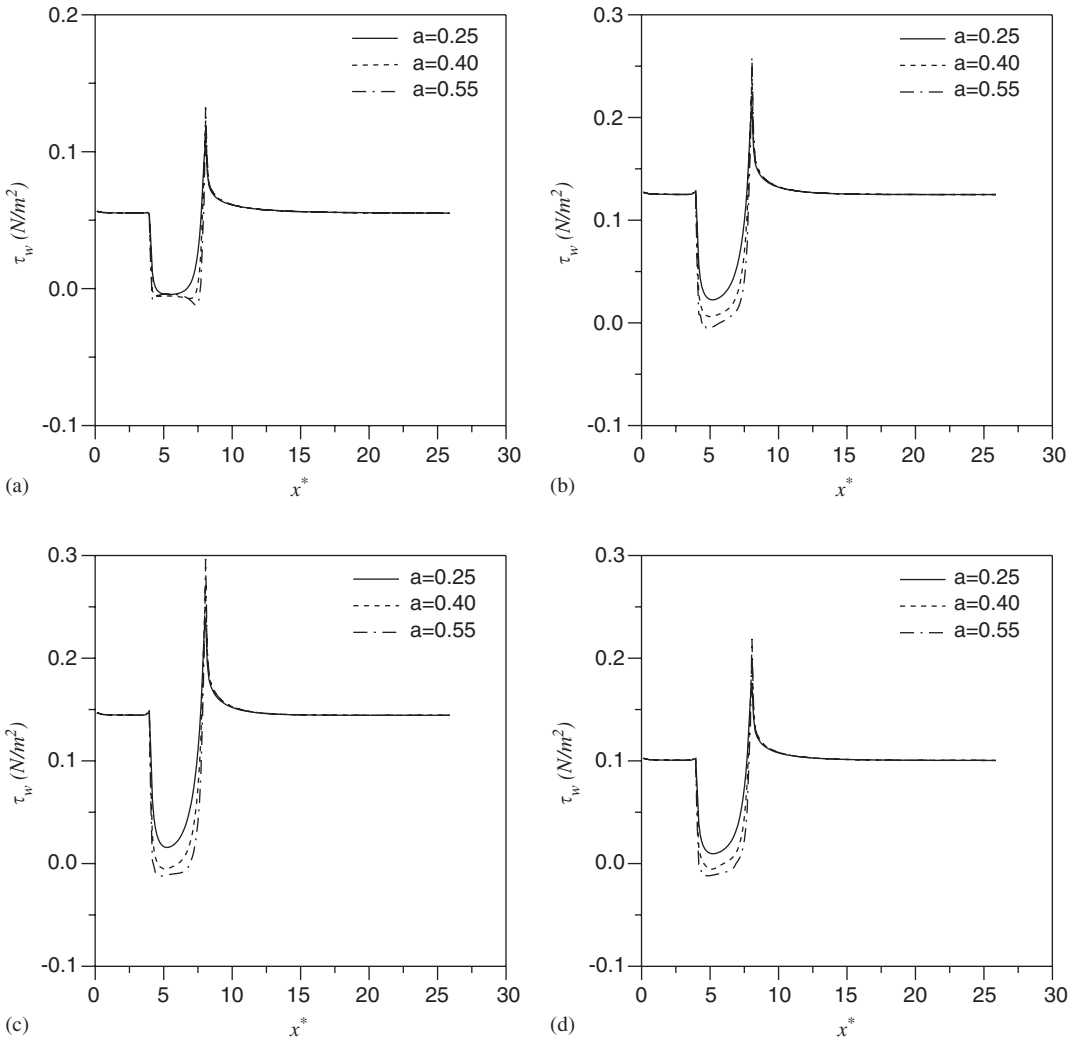

Figure 14. WSS distribution for different aneurysm widths for: (a) Newtonian; (b) Casson; (c) Power-Law; and (d) Quemada models.

5. CONCLUSIONS

A study of the flow effects of three different blood rheological models namely the Casson, Power-Law and Quemada models in 3D models of an axisymmetric stenosis and an aneurysm is presented. The flow field and wall shear-stress distributions that each model induces for different *Re* number and degrees of abnormality is investigated and results show that there are marked differences between simulating the blood as Newtonian and as non-Newtonian fluid. Furthermore in the case of the stenosis, the Power-Law model exhibits similar trends as the

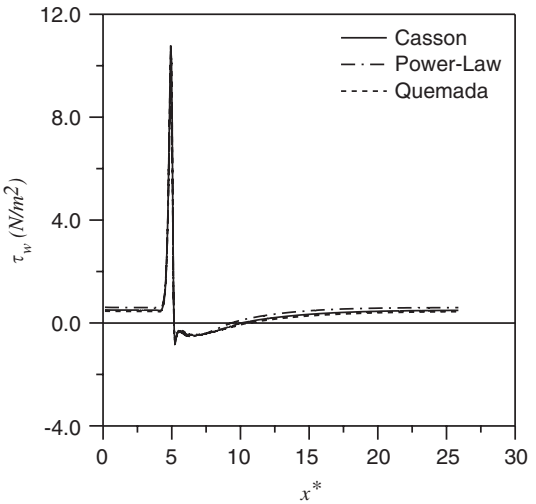

Figure 15. WSS distribution for 50% degree of stenosis and $Re = 300$ for all models.

Quemada and Casson models as regards the pressure difference when Re is varied whereas this trend is different as regards to the WSS. For low degrees of stenosis the pressure difference and WSS peaks for the Power-Law model are higher than for the other models. This phenomenon reverses for high degrees of stenosis. As regards the aneurysm case, the Power-Law model exhibits the highest values of maximum wall shear stress (τ_W^{max}) and pressure drop (ΔP) compared to the other models whereas the values of the minimum wall shear stress (τ_W^{min}) are very close for all models. In addition the increase of Re induces a more rapid increase of τ_W^{max} for the Power-Law model compared to the rest of the models whereas the increase in aneurysm bulging has virtually no effect on neither ΔP nor the wall shear stress distribution on any of the models. As regards the constitutive equations of the models, the Power-Law and Quemada models do not account for a yield stress, which is evident in rheological experiments of blood [25]. Therefore, the use of the Casson model should be preferred for modelling of low shear-rate flows. However, in some cases and for more complex flows the results for Quemada and Casson models at low shear-rate regions are very close. For example for the flow in a 50% degree of stenosis and for $Re = 300$, the flow reattachement points where shear rate is zero seem to be very close for the Quemada and Casson models (Figure 15) whereas the reattachement point for the Power-Law model appears at a shorter distance. Conclusively the Power-Law model exhibits different behaviour in all cases compared to the other models whereas Quemada and Casson models exhibit similar behaviour in the case of the stenosis but different behaviours in the case of the aneurysm.

REFERENCES

1. Ku DN. Blood flow in arteries. *Annual Review of Fluid Mechanics* 1997; **29**:399–434.
2. Ang KC, Mazumdar JN. Mathematical modelling of three-dimensional flow through an asymmetric arterial stenosis. *Mathematical and Computer Modelling* 1997; **25**:19–29.
3. Dvinsky AS, Ojha M. Simulation of three-dimensional pulsatile flow through an asymmetric stenosis. *Medical and Biological Engineering and Computing* 1994; **32**:138–142.

4. Bethier B, Bouzerar R, Legallais C. Blood flow patterns in an anatomically realistic coronary vessel: influence of three reconstruction methods. *Journal of Biomechanics* 2002; **35**:1347–1356.
5. Long Q, Xu XY, Ranmarine KV, Hoskins P. Numerical investigation of physiologically realistic pulsatile flow through arterial stenoses. *Journal of Biomechanics* 2001; **34**:1229–1242.
6. Tang D, Yang C, Kobayashi S, Ku DN. Generized finite difference method for 3-D viscous flow in stenotic tubes with large wall deformation and collapse. *Applied Numerical Mathematics* 2001; **38**:49–68.
7. Deplano V, Siouffi M. Experimental and numerical study of pulsatile flows through stenosis: wall shear stress analysis. *Journal of Biomechanics* 1999; **32**:1081–1090.
8. Bluestein D, Gutierrez C, Londono M, Schoephoerster RT. Vortex shedding in steady flow through a model of an arterial stenosis and its relevance to mural platelet deposition. *Annals of Biomedical Engineering* 1999; **27**:763–773.
9. Oshima M, Torii R, Kobayashi T, Taniguchi N, Takagi K. Finite element simulation of blood flow in the cerebral artery. *Computer Methods in Applied Mechanics and Engineering* 2001; **191**:661–671.
10. Kumar BVR, Naidu KB. Hemodynamics in aneurysm. *Computers and Biomedical Research* 1996; **29**:119–139.
11. Kumar BVR. A space-time analysis of blood flow in 3D vessel with multiple aneurysms. *Computational Mechanics* 2003; **32**:16–28.
12. Yu SCM, Chan WK, Ng BTH, Chua LP. A numerical investigation of the steady and pulsatile flow characteristics in axi-symmetric abdominal aortic aneurysm models with some experimental evaluation. *Journal of Medical Engineering and Technology* 1999; **23**:228–239.
13. Yu SCM. Steady and pulsatile flow studies in abdominal aortic aneurysm models using particle image velocimetry. *International Journal of Heat and Fluid Flow* 2000; **21**:74–83.
14. Egelhoff CJ, Budwig RS, Elger DF, Khraishi TA, Johansen KH. Model studies of the flow in abdominal aortic aneurysms during resting and exercise conditions. *Journal of Biomechanics* 1999; **32**:1319–1329.
15. Salsac AN, Sparks SR, Lasheras JC. Hemodynamic changes occurring during progressive enlargement of abdominal aortic aneurysms. *Annals of Vascular Surgery* 2004; **18**:14–21.
16. Viswanath N, Rodkiewicz CM, Sajac S. On the abdominal aortic aneurysms: pulsatile state considerations. *Medical Engineering and Physics* 1997; **19**:343–351.
17. Buchanan Jr JR, Kleinstreuer C, Comer JK. Rheological effects on pulsatile hemodynamics in a stenosed tube. *Computers and Fluids* 2000; **29**:695–724.
18. Pontrelli G. Blood flow through an axisymmetric stenosis. *Proceedings of the Institution of Mechanical Engineers Part H—Journal of Engineering in Medicine* 2001; **215**:1–10.
19. Neofytou P, Drikakis D. Effects of blood models on flows through a stenosis. *International Journal for Numerical Methods in Fluids* 2003; **43**:597–635.
20. Neofytou P. Comparison of blood rheological models for physiological flow simulation. *Biorheology* 2004; **41**:693–714.
21. Casson NA. A flow equation for pigment-oil suspensions of the printing ink type. In *Rheology of Disperse Systems*, Mills CC (ed.). Pergamon Press: New York, 1959; 84–102.
22. Walburn FJ, Schneck DJ. A constitutive equation for whole human blood. *Biorheology* 1976; **13**:201–210.
23. Quemada D. Rheology of concentrated disperse systems III. General features of the proposed non-Newtonian model. Comparison with experimental data. *Rheologica Acta* 1978; **17**:643–653.
24. Papanastasiou TC. Flow of materials with yield. *Journal of Rheology* 1987; **31**:385–404.
25. Charm SE, McComis W, Kurland G. Rheology and structure of blood suspension. *Journal of Applied Physiology* 1964; **19**:127–133.
26. Neofytou P, Drikakis D. Non-Newtonian flow instability in a channel with a sudden expansion. *Journal of Non-Newtonian Fluid Mechanics* 2003; **111**:127–150.
27. Leonard BP. A stable and accurate convective modelling procedure based on quadradic upstream interpolation. *Computer Methods in Applied Mechanics and Engineering* 1979; **19**:59–98.
28. Stone HL. Iterative solution of implicit approximations of multidimensional partial differential equations. *SIAM Journal on Numerical Analysis* 1968; **5**:530–558.
29. Davies PF. Flow-meditated endothelial mechanotransduction. *Physiological Reviews* 1995; **75**:519–560.
30. Budwig R, Elger D, Hooper H, Slippy J. Steady flow in abdominal aortic aneurysm models. *ASME Journal of Biomechanical Engineering* 1993; **115**:418–423.

